SCIENCE CHINA
Information Sciences

• RESEARCH PAPER •

May 2026, Vol. 69, Iss. 5, 152301:1–152301:21
https://doi.org/10.1007/s11432-025-4705-7

Exploring Hannan limitation for 3D antenna array

Ran JI[1], Chongwen HUANG[1*], Xiaoming CHEN[2], Wei E. I. SHA[1], Zhaoyang ZHANG[1], Jun YANG[3], Kun YANG[4], Chau YUEN[5] & Mérouane DEBBAH[6]

[1]*College of Information Science & Electronic Engineering and Zhejiang Key Laboratory of Multimodal Communication Networks and Intelligent Information Processing, Zhejiang University, Hangzhou 310027, China*
[2]*College of Information and Communication Engineering, Xi'an Jiaotong University, Xi'an 710049, China*
[3]*ZTE Corporation, Shenzhen 518000, China*
[4]*Vivo Mobile Communication Co., Ltd., Beijing 100015, China*
[5]*School of Electrical and Electronics Engineering, Nanyang Technological University, Singapore 639798, Singapore*
[6]*6G Research Center Computer and Information Engineering, Khalifa University, Abu Dhabi 127788, United Arab Emirates*

Received 14 May 2025/Revised 14 September 2025/Accepted 3 December 2025/Published online 18 March 2026

Abstract Hannan limitation describes the array performance limit for large 2D planar antenna arrays and demonstrates the inevitable radiation efficiency degradation caused by mutual coupling effects between array elements. However, this limitation is derived based on the assumption of infinitely large 2D arrays, which means that it is not an accurate law for small size arrays. In this paper, we extend this theory and propose an estimation formula for the radiation efficiency upper limit of finite-sized 2D arrays. Furthermore, we analyze a 3D array structure consisting of two parallel 2D arrays. Specifically, we provide evaluation formulas for the mutual coupling strengths for both infinite and finite-size 3D arrays and derive the fundamental efficiency limit of 3D arrays. Moreover, based on the established gain limit of antenna arrays with fixed aperture sizes, we derive the achievable gain limit of finite-size 3D arrays. Besides the performance analyses, we also investigate the spatial radiation characteristics of the considered 3D array structure, offering a feasible region for beamforming phase settings under a given energy attenuation threshold. Through simulations, we demonstrate the effectiveness of our proposed theories and gain advantages of 3D arrays for better spatial coverage under various scenarios.

Keywords 3D antenna array, efficiency limit, gain limit, 3D beamforming, Hannan limitation

Citation Ji R, Huang C W, Chen X M, et al. Exploring Hannan limitation for 3D antenna array. Sci China Inf Sci, 2026, 69(5): 152301, https://doi.org/10.1007/s11432-025-4705-7

1 Introduction

Multiple-input-multiple-output (MIMO) technologies have advanced significantly in 4G and 5G communications, proving to be an effective means of enhancing communication rates and reliability, and driving substantial progress in the field. However, theoretical analysis in electromagnetic (EM) and antenna theories suggests that the maximum array gain of a planar array is only dependent on the array aperture size, expressed as $G_{\max} = \frac{4\pi}{\lambda^2} A_p$, where A_p represents the physical area of the aperture and λ is the wavelength [1, Eq. (12-37)]. Although this result is derived for a constant distribution aperture, it is equally applicable to arbitrary 2D arrays. While expanding the aperture size of planar arrays to increase the number of antennas can enhance system performance, practical constraints such as the physical sizes of base stations, wind resistance, and hardware costs impose an upper limit on the size of the antenna array's aperture area. Additionally, for large 2D arrays, the directivity during beamforming across different spatial directions follows the variation $D = D_{\max} \cos\theta$ ([1, Eq. (6-103)] and [2]), where θ represents the angle between the beamforming direction and the vector perpendicular to the planar array. The $\cos\theta$ factor accounts for the decrease in directivity due to the decrease in the projected area of the array. For practical arrays, the array gain is equal to the directivity multiplied by the array radiation efficiency ($G = \eta D$, where η represents the array radiation efficiency). Therefore, the array gain for edge users is significantly reduced, leading to poorer service quality. Due to the aforementioned problems, it is natural to think if it is possible to further facilitate MIMO communications and augment the proven benefits of multi-antenna technologies.

* Corresponding author (email: chongwenhuang@zju.edu.cn)

1.1 Prior work

Several technologies have been developed to improve MIMO communications due to their successful implementations [3–5]. These include massive MIMO communications [6–15], reconfigurable intelligent surface (RIS) aided MIMO communications [16–26], and the recently emerged holographic MIMO (HMIMO) communications [27–32], which is developed from the concept of massive MIMO by integrating an immense (potentially infinite) number of antennas into a compact space [31]. Specifically, RIS has been demonstrated to have the capability to improve wireless signal coverage [33, 34]. Moreover, recent advancements in HMIMO communications can partially address the aforementioned issues due to the new physical properties in HMIMO systems, such as EM coupling effects and reconfigurable antenna elements [35]. These new properties enable improved array performance at large radiation angles through superdirectivity [36,37], thus partially resolving the aforementioned challenges. Refs. [35,38,39] have provided a comprehensive introduction to the emerging HMIMO wireless communications, particularly highlighting the HMIMO near-field communications, theoretical foundations, hardware architectures, and enabling technologies. However, although these emerging technologies can partially address the current issues, their primary objectives remain to enhance the overall performance of communication systems.

Another significant challenge faced by emerging technologies in MIMO arrays is that their achievable gain remains constrained by the array aperture area [40–46]. Hannan [47] investigated the limits of radiation efficiency for antenna elements in an infinitely large planar array and introduced the concept of embedded element efficiency. For antenna arrays with element spacing less than or equal to half a wavelength, the upper bound of the radiation efficiency for each element is given by $\frac{\pi A_e}{\lambda^2}$, where A_e denotes the physical area of an individual antenna element. This expression reflects an important physical constraint: under a fixed total aperture area A_p, increasing the number of antenna elements reduces the area of each element and intensifies mutual coupling effects between them. As a result, the radiation efficiency of each element decreases proportionally. Consequently, further reducing the element spacing below half a wavelength—although allowing more antennas to be placed within the same aperture—does not lead to higher total array gain, as the gain saturates due to efficiency degradation. Subsequent studies such as [48, 49] have verified through numerical measurements the good approximation of the embedded element efficiency method for large practical 2D arrays and its utility in design and numerical analysis. Wasylkiwskyj et al. [50–53] extended research on radiation efficiency issues for different antenna arrays, including linear arrays, finite excitation arrays, and grating lobe arrays, among others. Furthermore, besides radiation efficiency, other performance indicators such as the degrees of freedom (DoF) and achievable gain of antenna arrays are also constrained by the aperture area [40, 44].

Consequently, it is logical to consider whether applying 3D antenna arrays can break the gain limitations of planar arrays and improve beamforming capabilities for edge users, thus enhancing the overall performance and full-space coverage capabilities of the antenna array. Refs. [54–56] have investigated the directivity and effective area of 3D antenna arrays with different geometric structures. Specifically, for 3D arrays of standard geometric shapes, approximate analytical expressions have been proposed, and for more general arrangements of arbitrary 3D array structures, more complex integral expressions have been provided. However, these analyses of 3D array performance focus solely on the array radiation characteristics corresponding to the geometric arrangement of ideal radiating elements. Usually, 100% radiation efficiency and isotropic radiation pattern assumption are adopted, which are not realistic in practical scenarios. Since the effects of inter-element coupling and radiation efficiency reduction are overlooked, the resulting directivity limits cannot accurately represent the array gain limits of practical arrays. In terms of system performance, Refs. [36, 57–59] have studied the communication performance of 3D arrays in both line-of-sight (LOS) and non-line-of-sight (NLOS) scenarios. Specifically, Refs. [57, 58] revealed the marginal effects of far-field LOS channels. Ji et al. [36] utilized the electromagnetic coupling effects of HMIMO arrays combined with the 3D array structure to achieve multiple superdirective beams in space and evaluated the spectral efficiency in NLOS scenarios, which can be applied to multi-beam or edge networks [60,61]. Yuan et al. [59] evaluated the DoF and capacity performances of a fabricated two-layer 3D array in both Rayleigh and 3GPP scenarios. Furthermore, the use of stacked intelligent hypersurfaces [29,62] for interlayer computation and signal processing tasks also shares some conceptual similarities with 3D antenna arrays. However, to the best of the authors' knowledge, no previous work has derived the performance upper bounds for 3D arrays.

1.2 Our contribution

In this paper, we extend the theoretical analysis of Hannan limitation and explore the performance limits for 3D arrays. Specifically, we first introduce the concept of beam feasible region for 2D uniform arrays and give the efficiency upper bound of finite-sized 2D arrays. Furthermore, we derive the fundamental efficiency and gain limit

for a two-layer 3D array structure. Moreover, for 3D antenna arrays, we also investigate their spatial radiation characteristics and present the 3D beam feasible region under a given energy attenuation threshold. The contributions of this paper are listed as follows.

• We investigate the efficiency upper bound for finite-dimensional 2D arrays and both the efficiency and gain limit for 3D arrays. Specifically, the extension from infinite to finite-size arrays is achieved by analogizing the relationship between the active reflection coefficients and mutual coupling coefficients of the antenna array to the 2D discrete Fourier transform (DFT). Through this process, we successfully express the mutual coupling strength of the antenna array as the sampled values of the active reflection coefficients at a finite number of points. Moreover, for 3D arrays, the gain limit is proportional to their average spatial projection area.

• For two-layer 3D arrays, we investigate their spatial radiation characteristics and energy attenuation properties under different phase configurations. We also derive the beam feasible regions of the 3D array under a given energy attenuation coefficient constraint.

• Simulation results are provided to validate our proposed theorems and the spatial radiation characteristic analysis of 3D arrays. Additionally, the results quantify the achievable gain of a typical two-layer 3D array structure compared to a planar 2D array (for example, 37.5% gain for $2\lambda \times 2\lambda$ aperture size with a 0.75λ inter-layer spacing).

The rest of this paper is organized as follows. In Section 2, a brief introduction to the derivation of the 2D array efficiency limit is given. Next, theoretical analyses are carried out in Section 3 to extend the aforementioned methods to the evaluation of the efficiency for finite-dimensional 2D arrays. In Section 4, efficiency and gain limits for two-layer 3D arrays are provided. After that, the spatial radiation characteristics of two-layer 3D arrays are investigated in Section 5, and the corresponding spatial feasible region is also presented. Simulation results are provided in Section 6 to validate our theoretical analyses and the performance gain of a practical 3D array. Finally, some remarks and conclusion are given in Section 7.

2 Performance limit of 2D array

Hannan [47] introduced in 1964 the embedded element efficiency concept that explained the so-called element-gain paradox in planar antenna arrays, i.e., that the array gain is always smaller than the sum of the element gain. Subsequent studies [48, 49] further demonstrated the effectiveness of this approach by evaluating the directivities and aperture efficiencies of planar arrays composed of open-ended waveguides and dipoles, respectively, across a wide range of element spacings. Specifically, the theoretical value for the embedded element efficiency theory lies in the fact that for $M \times N$ planar array elements, the array gain can be found as MN times the element gain of the embedded element when the embedded element efficiency is included in the element gain model. Moreover, a similar conclusion in a more general form was summarized in [63]. The most important conclusion of these developments is that for a planar array of identical elements situated in identical array environments (i.e., idempotent array), and with the same phase shift in adjacent antenna elements, a necessary amount of mutual coupling must exist among the elements of the array, which can be overall represented by the element efficiency parameter. In the following part of this section, we will provide a brief overview of Hannan's derivation approach and explicitly outline the constraint conditions associated with the aforementioned conclusions. This will serve as a foundation for extending these findings to the finite 2D array and 3D array scenarios in the following sections.

2.1 Array reflection and radiation

We first consider an infinitely large 2D planar antenna array, as illustrated in Figure 1. For 2D cases, only layer 1 exists, and we adopt the concepts of coupling and energy reflection coefficients introduced in [47]. The coupling coefficient C_{pq} can be defined through the following process in Figure 1(b): by exciting a single element and measuring the reflected energy at all ports, the coupling coefficient is defined as the ratio of the signal reflected at the receiver to the signal available at the generator. This coefficient is generally a complex coupling coefficient, as both the amplitude and the phase are measured. Based on the definition of the coupling coefficient, the energy reflection coefficient can be defined through the symmetrical process shown in Figure 1(a): when the entire array is excited with a linear phase difference of α along the x-axis and β along the y-axis, the ratio of the signal reflected at the reference antenna to the signal available at the generator is measured. Finally, the coupling and energy

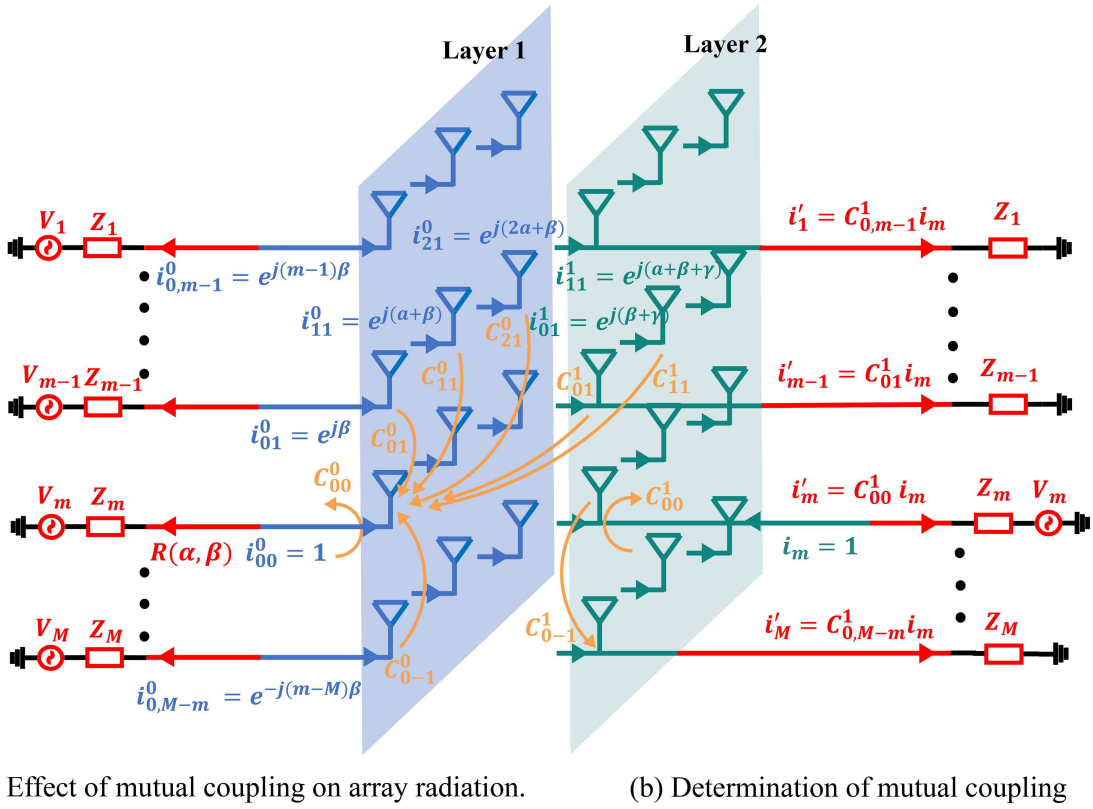

Figure 1 (Color online) (a) Effect of mutual coupling on array radiation and (b) determination of mutual coupling.

reflection coefficients are related by the following equation due to reciprocity and superposition:

$$\begin{aligned} R(\alpha,\beta) &= \sum_{p=-\infty}^{+\infty}\sum_{q=-\infty}^{+\infty} C_{pq} e^{j(p\alpha+q\beta)} \\ &\overset{(a)}{=} \sum_{p=-\infty}^{+\infty}\sum_{q=-\infty}^{+\infty} C_{pq}\cos\left(p\alpha+q\beta\right), \end{aligned} \tag{1}$$

which corresponds to the physical interpretation that the reflected signal $R(\alpha,\beta)$ is the sum of the products of the coupling coefficients and the corresponding generator phase factors. Moreover, C_{pq} represents the array coupling coefficients relative to the reference antenna point, where p is the column index and q is the row index, respectively. Eq. (a) is due to symmetry $C_{pq} = C_{-p-q}$ in infinitely large arrays.

Eq. (1) is essentially a 2D Fourier series. Therefore, Parseval's theorem can be used to establish the energy relationship between the reflection coefficients and the coupling coefficients as follows:

$$\frac{1}{\pi^2}\int_{\alpha=0}^{\pi}\int_{\beta=0}^{\pi} \left|R\left(\alpha,\beta\right)\right|^2 d\alpha d\beta = \sum_{p=-\infty}^{+\infty}\sum_{q=-\infty}^{+\infty} \left|C_{pq}\right|^2, \tag{2}$$

which means that the average power returned to a transmitter in a fully operational array is equal to the net power returned to all transmitters when only one transmitter is excited (the power is averaged over the angle range [0, π]). Moreover, based on the above energy relationship, an expression for the reduction in radiation efficiency due to mutual coupling can be provided [47]:

$$\begin{aligned} \eta &= 1 - \sum_{p=-\infty}^{+\infty}\sum_{q=-\infty}^{+\infty} \left|C_{pq}\right|^2 \\ &= 1 - \frac{1}{\pi^2}\int_{\alpha=0}^{\pi}\int_{\beta=0}^{\pi} \left|R\left(\alpha,\beta\right)\right|^2 d\alpha d\beta. \end{aligned} \tag{3}$$

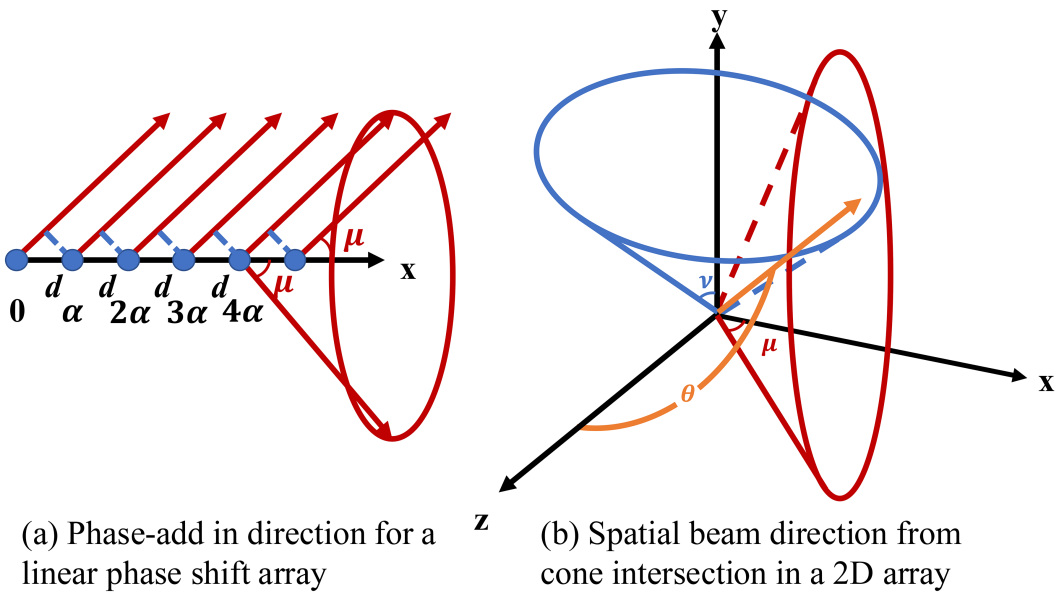

(a) Phase-add in direction for a linear phase shift array

(b) Spatial beam direction from cone intersection in a 2D array

Figure 2 (Color online) 2D array spatial radiation characteristics.

2.2 2D feasible region

In this subsection, we establish the concept of the beam feasible region for a 2D array and introduce the ideal properties of $R(\alpha,\beta)$ based on this. First, for a linear array along the x-axis, the linear phase difference α creates an add-in phase direction in space with an angle μ to the x-axis, as shown in Figure 2(a). The relationship between them is given by

$$\alpha = -2\pi\frac{d_x\cos\mu}{\lambda}, \tag{4}$$

where d_x is the antenna interspace. Obviously, the direction of phase coherence addition forms a conical shape in space for the linear array. For a 2D array, the phase differences α and β along the x-axis and y-axis, respectively, form two cones with angles μ and ν to the x-axis and y-axis. If these two cones do not intersect, it means the 2D array cannot radiate energy in any direction in space (for an infinitely large array). Conversely, if they do intersect, there exists a spatial radiation direction for the 2D array, as shown in Figure 2(b). From the geometric relationship of the figure, it is evident that $\cos^2\mu+\cos^2\nu=\sin^2\theta$. Therefore, the feasible beam domain of the 2D array can be defined as

$$\cos^2\mu+\cos^2\nu\leqslant 1\Rightarrow\left(\frac{\lambda\alpha}{2\pi d_x}\right)^2+\left(\frac{\lambda\beta}{2\pi d_y}\right)^2\leqslant 1. \tag{5}$$

Based on the above analysis, a reasonable assumption for the reflection coefficient $R(\alpha,\beta)$ proposed in [47] is that $R(\alpha,\beta)=0$ in the feasible region, and $R(\alpha,\beta)=1$ in the non-feasible region where the infinite array cannot effectively radiate. The underlying physical reason is as follows: for an infinite 2D array, the spatial radiation beam is infinitely narrow within the feasible region, and its spatial beam shape can be approximately considered equal. However, there is no radiation beam in space outside the feasible region since coherent phase radiation directions cannot be formed. Ultimately, when there are no grating lobes, the average radiation efficiency limit of an infinite 2D array is

$$1-\frac{1}{\pi^2}\iint_0^{\pi}R(\alpha,\beta)d\alpha d\beta=\frac{\pi d_x d_y}{\lambda^2}. \tag{6}$$

The significance of this radiation efficiency limit expression lies in its connection between the ideal radiation pattern of a 2D planar array (with a $\cos\theta$ shape and directivity equal to 4) and the maximum achievable gain expression of the antenna array ($\frac{4\pi A_p}{\lambda^2}$). It indicates that the reduction in radiation efficiency due to mutual coupling remains unavoidable.

3 Radiation efficiency of 2D finite arrays

As described in Section 2, Hannan established two insightful formulas: the relationship between the coupling and reflection coefficients (1), and their corresponding energy relationship (2), which are essentially a 2D discrete-time Fourier transform (DTFT) and the corresponding Parseval's theorem as shown below:

$$\begin{cases} \text{DTFT}: X(e^{j\omega_1}, e^{j\omega_2}) = \sum_{m=-\infty}^{\infty} \sum_{n=-\infty}^{\infty} x[m,n] e^{-j(\omega_1 m + \omega_2 n)}, \\ \\ \text{Parseval's theorem}: \frac{1}{(2\pi)^2} \int_0^{2\pi} \int_0^{2\pi} \left| X\left(e^{j\omega_1}, e^{j\omega_2}\right) \right|^2 d\omega_1 \, d\omega_2 = \sum_{m=-\infty}^{\infty} \sum_{n=-\infty}^{\infty} |x[m,n]|^2, \end{cases} \tag{7}$$

$$\begin{cases} \text{2D Array}: R(\alpha, \beta) = \sum_{p=-\infty}^{+\infty} \sum_{q=-\infty}^{+\infty} C_{pq} e^{j(p\alpha + q\beta)}, \\ \\ \text{Parseval's theorem}: \frac{1}{\pi^2} \int_{\alpha=0}^{\pi} \int_{\beta=0}^{\pi} |R(\alpha, \beta)|^2 \, d\alpha d\beta = \sum_{p=-\infty}^{+\infty} \sum_{q=-\infty}^{+\infty} |C_{pq}|^2. \end{cases} \tag{8}$$

By comparing the above equations, it can be observed that the coupling term C_{pq} is equivalent to the values of the $x[m,n]$ signal. Based on this observation of mathematical formulas and the corresponding physical mapping, we can extend the radiation efficiency limits of a 2D infinite planar antenna array to the case of a finite 2D array by analogizing the derivation process from the DTFT to the DFT. This allows us to estimate the radiation efficiency upper limit of a finite-size array. To simplify the analysis, we illustrate this approach using the 1D DTFT and DFT formulas as an example. The 2D DTFT and DFT transformations can be similarly analogized. The formula transition from 1D DTFT to 1D DFT is

$$\text{DTFT} \begin{cases} X(\omega) = \sum_{n=-\infty}^{\infty} x[n] e^{-j\omega n}, \\ \\ x[n] = \dfrac{1}{2\pi} \int_0^{2\pi} X(\omega) e^{j\omega n} d\omega, \end{cases} \Rightarrow \text{DFT} \begin{cases} X(k) = \sum_{n=0}^{N-1} x[n] e^{-j\frac{2\pi}{N} kn}, \\ \\ x[n] = \dfrac{1}{N} \sum_{k=0}^{N-1} X(k) e^{j\frac{2\pi}{N} kn}, \end{cases} \tag{9}$$

when the time-domain sampled signal $x[n]$ changes from infinite to finite N points, its frequency-domain characteristics are compressed from being describable at arbitrary points to being described at the sampled points $X(\omega = \frac{2\pi k}{N}), k \in \{0, 1, \ldots, N-1\}$. Recall that we consider the time-domain sampled signal $x[n]$ in the equation as equivalent to the coupling terms in the analyzed antenna array scenario; therefore, the finite N-point DFT essentially corresponds to the relationship between the coupling and reflection coefficients of a finite-dimensional antenna array. By replacing the time-frequency variables in the 2D DFT formulation with the corresponding parameters of a 2D finite array, the reflection coefficients of an infinite 2D array can be rewritten for a finite 2D array as follows:

$$R(\alpha, \beta) = \sum_{p=-\infty}^{+\infty} \sum_{q=-\infty}^{+\infty} C_{pq} e^{j(p\alpha + q\beta)} \Rightarrow \mathcal{R}_{00}(m,n) = \sum_{p=0}^{M-1} \sum_{q=0}^{N-1} C_{pq} e^{j\left(\frac{2\pi m}{M} p + \frac{2\pi n}{N} q\right)}, \tag{10}$$

where M and N represent the number of antenna elements along the x-axis and y-axis of the 2D array, respectively, and $\mathcal{R}(m,n)$ represents the sampling point of $R(\alpha, \beta)$ at $(\alpha = \frac{2\pi m}{M}, \beta = \frac{2\pi n}{N})$. The subscript (0, 0) indicates that the point at the bottom left of the 2D array in Figure 1(a) is selected as the reference point. In this case, the values of the coupling coefficient subscript (p, q) are positive. Clearly, if another point in the array is chosen as the reference point, the range of values for (p, q) will differ. The corresponding new energy relationship is

$$\sum_{p=0}^{M-1} \sum_{q=0}^{N-1} |C_{pq}|^2 = \frac{1}{MN} \sum_{m=0}^{M-1} \sum_{n=0}^{N-1} |\mathcal{R}_{00}(m,n)|^2. \tag{11}$$

However, for finite-dimensional arrays, we essentially focus only on the overall performance of the array. Therefore, by denoting the overall reflection coefficient of the finite array as $\mathcal{R}(m,n)$, we have the following relationship:

$$\sum_{p=0}^{M-1} \sum_{q=0}^{N-1} \left|\overline{C}_{pq}\right|^2 = \frac{1}{MN} \sum_{m=0}^{M-1} \sum_{n=0}^{N-1} |\mathcal{R}(m,n)|^2, \tag{12}$$

where $\left|\overline{C}_{pq}\right|$ represent the average coupling strengths of the finite array. As an example, we show the sampling points of a 10×10 2D array in Figure 3.

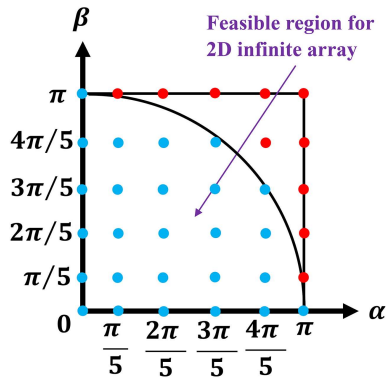

Figure 3 (Color online) Sampling points for a finite dimension 2D array. Blue/red dots represent beamforming sampling points in/out the 2D feasible region, respectively.

Theorem 1. Element efficiency for a finite 2D array can be formulated as

$$\begin{aligned}\eta &= 1 - \sum_{p=0}^{M-1}\sum_{q=0}^{N-1}\left|\overline{C}_{pq}\right|^2 \\ &= 1 - \frac{1}{MN}\sum_{m=0}^{M-1}\sum_{n=0}^{N-1}\left|R\left(\frac{2\pi m}{M}, \frac{2\pi n}{N}\right)\right|^2.\end{aligned} \tag{13}$$

Remark 1. From Theorem 1, we can transform the problem of estimating the performance limit of a finite 2D antenna array into the problem of estimating the reflected energy at the discrete sampling points, which is further investigated in the following subsections.

3.1 Feasible sampling points

When the discrete sampling points are within the feasible region of the 2D antenna array (as indicated by the blue points in Figure 3), the 2D array has a main radiation direction with coherent phase addition in space. Therefore, for a 2D array composed of ideal antenna elements without ohmic losses, we can adopt the assumption consistent with Hannan [47]: the reflection coefficient R equals zero inside the feasible region, i.e., $\mathcal{R}(m,n)=0$.

3.2 Infeasible sampling points

When the discrete sampling points are outside the feasible region (as indicated by the red points in Figure 3), the radiation characteristics of the finite 2D array differ from those of an infinite 2D array. For a finite array, sampling points outside the feasible region do not lead to zero spatial radiation energy. Therefore, a correct assessment of the radiation efficiency upper limit for a finite 2D array requires further study of the array reflection coefficients corresponding to sampling points outside the feasible region. However, accurately estimating the active reflection coefficient of a finite 2D antenna array under arbitrary excitation conditions is a challenging problem in the fields of electromagnetics and antenna design. In practical scenarios, the commonly used approaches to achieve this are still full-wave electromagnetic simulations or actual measurements, as exemplified by [64, 65]. In order to achieve a relatively accurate estimate of the sampling points outside the feasible region without excessively exaggerating the upper limit of the radiation efficiency for finite-size 2D arrays, we adopt the active reflection coefficient model proposed in [50], where only a finite number of antenna elements are excited in an infinite plane. Compared to the finite 2D array under the same settings, this scenario results in more severe ohmic losses and coupling effects for each antenna excitation generator, thereby reducing radiation efficiency. Thus, applying this model represents a more conservative estimate of the upper limit of the radiation efficiency for a finite 2D array.

The estimation formula of reflection coefficients $R(\alpha,\beta)$ for $M\times N$ 2D finite excitation elements in [50] can be written as

$$|R(\alpha,\beta)|^2 = \frac{1}{(2\pi)^2}\int_{-\pi}^{\pi}\int_{-\pi}^{\pi}|R(\varrho,\zeta)|^2\left|A^{(MN)}(\varrho,\zeta;\alpha,\beta)\right|^2 d\varrho d\zeta, \tag{14}$$

where $R(\varrho,\zeta)$ represents the standard reflection coefficient of infinitely large planar arrays (i.e., zero in the feasible region and one in the non-feasible region). Moreover, the excitation function can be defined as

$$A^{(MN)}(\varrho,\zeta;\alpha,\beta)=\sum_{m=-\infty}^{+\infty}\sum_{n=-\infty}^{+\infty}a_m b_n e^{-j(m\varrho+n\zeta)}. \tag{15}$$

For an $M\times N$ finite-dimensional array, we apply

$$\begin{aligned} a_m&=\begin{cases}\frac{1}{\sqrt{MN}}e^{jm\alpha}, & |m|\leqslant\frac{M-1}{2},\\ 0, & |m|>\frac{M-1}{2},\end{cases}\\ b_n&=\begin{cases}\frac{1}{\sqrt{MN}}e^{jn\beta}, & |n|\leqslant\frac{N-1}{2},\\ 0, & |n|>\frac{N-1}{2},\end{cases}\end{aligned} \tag{16}$$

and the excitation function can be written as

$$\left|A^{(MN)}(\varrho,\zeta;\alpha,\beta)\right|=\frac{\sin\left[(M/2)(\alpha-\varrho)\right]\sin\left[(N/2)(\beta-\zeta)\right]}{\sqrt{MN}\sin\left[(\alpha-\varrho)/2\right]\sin\left[(\beta-\zeta)/2\right]}, \tag{17}$$

where $\left|A^{(MN)}(\varrho,\zeta;\alpha,\beta)\right|$ represents the Fourier transform projection component of the finite excitation sequence a_m and b_n onto the standard infinite uniform excitation (ϱ,ζ). Essentially, the above formula connects the reflection coefficients of finite and infinite arrays through the projection coefficients. Finally, by substituting the estimated reflection coefficients $R(\alpha,\beta)$ for the sampling points in the infeasible region in (13), we can obtain the efficiency upper bound for finite 2D antenna arrays. In the next section, we extend the analysis results for 2D antenna arrays to 3D cases and provide the efficiency and gain limits for 3D arrays.

4 Performance analyses of 3D arrays

Without loss of generality, the following analysis mainly focuses on two-layer 3D antenna arrays. This is due to their practical feasibility under hardware complexity and fabrication constraints. However, the proposed analytical approach can be generalized to multi-layer 3D arrays.

4.1 Efficiency analyses

In this section, we focus on a two-layer 3D antenna array structure, where each layer is a 2D antenna array as analyzed in Section 2. First, we analyze the case of infinite 2D arrays. Then, the discrete sampling method used to transition from infinite arrays to finite arrays can be similarly applied to analyze the performance limits of a finite 3D array. For the 3D array structure, we define its spatial radiation characteristics using a total of six parameters, divided into two groups: (α,β,γ) and (μ,ν,ξ). Specifically, (α,β,γ) represent the linear phase changes between antenna elements along the (x,y,z) axes, respectively. The corresponding angles between the in-phase directions and the (x,y,z) axes are represented by (μ,ν,ξ), as shown in Figure 4.

When the beam of the operating array antenna scans the space by varying the phases of element excitations, the presence of mutual coupling causes the signal reflected into each generator to vary. If all the coupling coefficients are available, the characteristics of the reflection signal versus the excitation phases can be computed. This is done simply by adding together the signals from all the generators as they are coupled back into one generator, as suggested in Figure 1(a). Thus, by reciprocity and superposition, the reflection coefficient of the considered 3D antenna array can be written as

$$R(\alpha,\beta,\gamma)=\sum_{p=-\infty}^{+\infty}\sum_{q=-\infty}^{+\infty}\left[C_{pq}^{0}e^{j(p\alpha+q\beta)}+C_{pq}^{1}e^{j(p\alpha+q\beta+\gamma)}\right], \tag{18}$$

where the coupling terms C_{pq}^{0} represent the mutual coupling coefficients between the reference antenna element and other antenna elements within the same 2D array plane, while C_{pq}^{1} represent the coupling coefficients between the reference antenna element and the elements in the other planar layer. The relationship between the reflection coefficients and the coupling coefficients is illustrated in Figure 1. Due to the geometrical symmetry, we have $C_{pq}^{0}=C_{-p-q}^{0}$ and $C_{pq}^{1}=C_{-p-q}^{1}$ in infinitely large 3D array cases. Thus, each pair of elements that are symmetrical about the reference element contributes a term equal to $C_{pq}^{0}\exp\left[j\left(p\alpha+q\beta\right)\right]+C_{-p-q}^{0}\exp\left[j\left(-p\alpha-q\beta\right)\right]=$

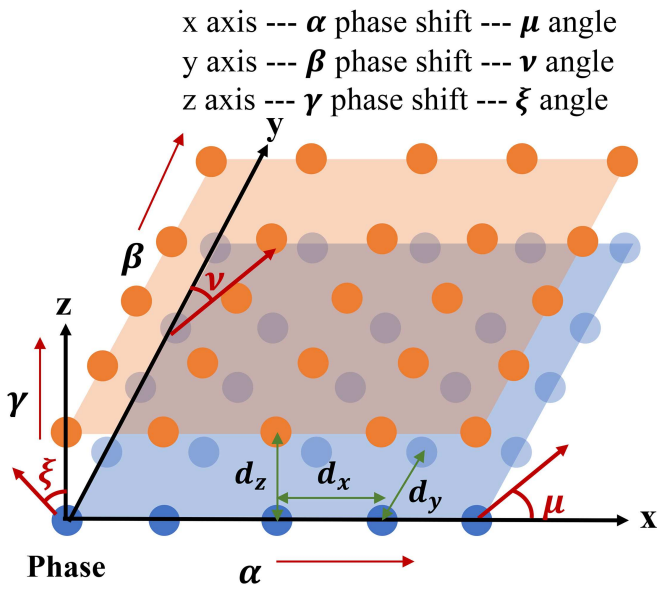

Figure 4 (Color online) Geometry of the considered two-layer 3D array.

$\left(C_{pq}^{0}+C_{-p-q}^{0}\right)\cos(p\alpha+q\beta)$. Similarly, the coupling between the reference antenna element and the elements of another planar antenna array follows the relationship

$$\begin{aligned}&C_{pq}^{1}\exp\left[j\left(p\alpha+q\beta+\gamma\right)\right]+C_{-p-q}^{1}\exp\left[j\left(-p\alpha-q\beta+\gamma\right)\right]\\&=\left(C_{pq}^{1}+C_{-p-q}^{1}\right)\cos(p\alpha+q\beta)\exp(j\gamma).\end{aligned}\tag{19}$$

By substituting the above symmetry relationships into the active reflection coefficient expression (18), we can obtain the following Fourier expansion:

$$R(\alpha,\beta,\gamma)=\sum_{p=-\infty}^{+\infty}\sum_{q=-\infty}^{+\infty}\left(C_{pq}^{0}+C_{pq}^{1}e^{j\gamma}\right)\cos\left(p\alpha+q\beta\right),\tag{20}$$

and the corresponding Parseval's theorem can be derived as

$$\begin{aligned}&\frac{1}{\pi^{2}}\iint_{0}^{\pi}\left|R(\alpha,\beta,\gamma)\right|^{2}d\alpha d\beta=\sum_{p=-\infty}^{+\infty}\sum_{q=-\infty}^{+\infty}\left|C_{pq}^{0}+C_{pq}^{1}e^{j\gamma}\right|^{2}\\&=\sum_{p=-\infty}^{+\infty}\sum_{q=-\infty}^{+\infty}\left(C_{pq}^{0}+C_{pq}^{1}e^{j\gamma}\right)\left(C_{pq}^{0*}+C_{pq}^{1*}e^{-j\gamma}\right)\\&=\sum_{p=-\infty}^{+\infty}\sum_{q=-\infty}^{+\infty}\left|C_{pq}^{0}\right|^{2}+\left|C_{pq}^{1}\right|^{2}+C_{pq}^{0}C_{pq}^{1*}e^{-j\gamma}+C_{pq}^{0*}C_{pq}^{1}e^{j\gamma},\end{aligned}\tag{21}$$

where the first two terms are the squared magnitudes of the coupling coefficients, representing the reflected power that limits the radiation efficiency upper bound of the 3D antenna array. Through further observation, it is evident that when the inter-layer phase difference is set as $\gamma=0$ and $\gamma=\pi$, the summation of the remaining two correlation terms can be written as

$$\begin{cases}C_{pq}^{0}C_{pq}^{1*}+C_{pq}^{0*}C_{pq}^{1}, & \gamma=0,\\[2ex] -C_{pq}^{0}C_{pq}^{1*}-C_{pq}^{0*}C_{pq}^{1}, & \gamma=\pi,\end{cases}$$

which can cancel each other out and be eliminated when summed. Therefore, by investigating the reflection coefficients of the 3D array under the conditions of $\gamma=0$ and $\gamma=\pi$, and then averaging the results, we can derive the expression for the radiation efficiency upper bound of the 3D antenna array.

Theorem 2. The embedded element efficiency for a two-layer infinite 3D array can be written as

$$\begin{aligned}\eta_{3D} &= 1 - \sum_{p=-\infty}^{+\infty}\sum_{q=-\infty}^{+\infty}\left(\left|C_{pq}^{0}\right|^2 + \left|C_{pq}^{1}\right|^2\right) \\ &= 1 - \frac{\frac{1}{\pi^2}\iint_0^{\pi}\left(\left|R(\alpha,\beta,0)\right|^2 + \left|R(\alpha,\beta,\pi)\right|^2\right)d\alpha d\beta}{2}.\end{aligned} \tag{22}$$

Remark 2. The significance of (22) lies in indicating the average radiation efficiency limit of a 3D array when performing beamforming across the entire space. Specifically, this requires considering γ as a parameter dependent on (α,β) to ensure that all antennas are in phase, and performing a double integral of (20) with (α,β) as variables. However, analytically solving this integral is quite difficult. Therefore, in the above analysis, we treat γ as a third free variable to obtain more intuitive theoretical analysis results. We have also performed numerical validations for (22) and (23).

Remark 3. For a two-layer 3D array, we only need to evaluate the reflection coefficients for the two cases where the phase differences along the z-axis are 0° and 180°. Then, by taking the average, we can obtain the average coupling intensity and radiation efficiency of the 3D array.

Remark 4. The physical interpretation of (22) is that the energy coupled to other ports will be absorbed by the load and will not be radiated.

Furthermore, we can apply a similar derivation process as in Section 3, where we transitioned from an infinite 2D antenna array to a finite 2D array. By discretely sampling the reflection coefficient plane $R(\alpha,\beta,\gamma)$, we can extend (22) to a finite 3D antenna array scenario as follows:

$$\begin{aligned}\eta_{3D}^{(MN)} &= 1 - \sum_{p=0}^{M-1}\sum_{q=0}^{N-1}\left(\left|\overline{C}_{pq}^{0}\right|^2 + \left|\overline{C}_{pq}^{1}\right|^2\right) \\ &= \frac{1}{2} - \frac{\sum_{m=0}^{M-1}\sum_{m=0}^{N-1}\left|R(\frac{2\pi m}{M},\frac{2\pi n}{N},0)\right|^2}{2MN} \\ &\quad + \frac{1}{2} - \frac{\sum_{m=0}^{M-1}\sum_{n=0}^{N-1}\left|R(\frac{2\pi m}{M},\frac{2\pi n}{N},\pi)\right|^2}{2MN}.\end{aligned} \tag{23}$$

Next, we conduct a more detailed analysis of the active reflection coefficient $R(\alpha,\beta,\gamma)$ of the considered 3D array structure. For infinitely large planar arrays, as analyzed earlier, there is no residual radiation in any out-of-phase condition since the major lobe occupies an infinitesimal angular region. Thus, infinitely large 3D arrays also exhibit radiation only in the main lobe direction. However, please note that the radiation beams from the two layers of the 3D array are not necessarily in-phase, depending on the setting of γ. Therefore, for the 3D array geometry shown in Figure 4, the radiation direction is determined by the phase pair (α,β), but the radiation efficiency is determined by all three parameters (α,β,γ). Specifically, the phase delay induced by the transmission of EM waves with an angle θ to the z-axis is

$$\delta_z = -2\pi\frac{d_z\cos\theta}{\lambda}. \tag{24}$$

With a phase difference of γ set between different layers, the phase difference between the beams from the two layers observed in the main lobe direction is

$$\varphi = \gamma - 2\pi\frac{d_z\cos\theta}{\lambda}. \tag{25}$$

Here, we assume that an ideal array can fully radiate its energy, yielding a reflection coefficient $R=0$ when phase alignment exists between the upper and lower layers, maximizing the main radiation beam. However, when a phase difference arises between these layers, a mismatch causes some energy to be reflected. In this case, the ratio of radiated energy to the maximum possible radiated energy is given by $\frac{\left|\boldsymbol{E}+\boldsymbol{E}e^{j\varphi}\right|^2}{4|\boldsymbol{E}|^2}$, and the corresponding active reflection coefficient can be written as

$$\left|R(\alpha,\beta,\gamma)\right|^2 = 1 - \frac{\left|1+e^{j\varphi}\right|^2}{4} \in D, \tag{26}$$

which corresponds to the percentage of energy that cannot be radiated, and D is the 2D feasible region defined in (5). The above analysis reveals the differences in spatial energy distribution between 3D and 2D arrays: for 2D arrays, energy is considered fully radiated if there is an in-phase radiation direction in space; otherwise, there is no radiation ($R(\alpha,\beta)$ only takes values of 0 or 1). However, the radiated energy varies with φ for 3D arrays, and the corresponding $R(\alpha,\beta,\gamma)$ can take values in the range of $[0,1]$. Based on (26), the average reflection coefficient for a fixed γ can be written as

$$\begin{aligned}\hat{R}(\gamma)&=\frac{1}{\pi^2}\iint_0^{\pi}\left|R(\alpha,\beta,\gamma)\right|^2 d\alpha d\beta\\&=1-\frac{1}{\pi^2}\iint_D\frac{1+\cos\varphi}{2}d\alpha d\beta\\&=1-\frac{\pi d_x d_y}{2\lambda^2}-\frac{1}{\pi^2}\iint_D\frac{\cos\left(\gamma-\frac{2\pi d_z\cos\theta}{\lambda}\right)}{2}d\alpha d\beta\end{aligned}\tag{27}$$

with $\cos\theta=\sqrt{1-\sin^2\theta}=\sqrt{1-\left(\frac{\lambda\alpha}{2\pi d_x}\right)^2-\left(\frac{\lambda\beta}{2\pi d_y}\right)^2}$. Furthermore, by substituting (27) into (22), we have the following corollary.

Corollary 1. The embedded element efficiency upper bound for a 3D array consisting of two parallel infinite planar uniform arrays can be formulated as

$$\begin{aligned}\eta_{3D}=&1-\frac{\frac{1}{\pi^2}\iint_0^{\pi}\left(\left|R(\alpha,\beta,0)\right|^2+\left|R(\alpha,\beta,\pi)\right|^2\right)d\alpha d\beta}{2}\\=&1-\frac{1-\frac{\pi d_x d_y}{2\lambda^2}-\frac{1}{\pi^2}\iint_D\frac{\cos\left(0-\frac{2\pi d_z\cos\theta}{\lambda}\right)}{2}d\alpha d\beta}{2}\\&-\frac{1-\frac{\pi d_x d_y}{2\lambda^2}-\frac{1}{\pi^2}\iint_D\frac{\cos\left(\pi-\frac{2\pi d_z\cos\theta}{\lambda}\right)}{2}d\alpha d\beta}{2}\\=&\frac{\pi d_x d_y}{2\lambda^2}=\frac{1}{2}\eta_{2D}.\end{aligned}\tag{28}$$

Remark 5. For infinitely large planar arrays, the embedded element efficiency of a 3D array decreases by half compared to an infinitely large 2D planar array due to the stronger coupling effects between the elements, as the 3D array has more antennas.

Remark 6. Physical explanation: the gain of a 3D array is essentially derived from the increased effective projected area in the vertical dimension when observed from non-broadside directions. However, for infinitely large planar arrays, regardless of the finite spacing between the two layers, the increased projected area in the vertical dimension can always be neglected when observing the array from angles other than the broadside direction. Therefore, for the observer, the effective area of the antenna array is the same, and thus the corresponding array gain limit is also the same. However, since the number of antennas has doubled, the average radiation efficiency decreases by half accordingly.

Remark 7. Although there is no benefit in forming a 3D array from infinitely large planar arrays, a finite-size 3D array can achieve an increased effective aperture area in space compared to corresponding 2D arrays, thereby obtaining benefits.

Until now, we have obtained an analytical solution for (22). However, it remains an open problem to analyze and compute the reflection coefficients for finite-dimensional 3D arrays under arbitrary configuration $R(\alpha,\beta,\gamma)$. Therefore, an analytical expression for (23) is difficult to establish. To address this issue, the next section provides an approximation expression for (23) from the perspective of the gain limit and verifies it through simulation.

4.2 Gain limit of finite aperture 3D antennas

As described in Section 2, the gain limit of large 2D arrays is proportional to the projected area of the antenna aperture in the observation direction and can be approximated by $\frac{4\pi A_p}{\lambda^2}\cos\theta$ [47]. For a rectangular 3D array with face areas $A_{xy}A_{xz},A_{yz}$, however, when observed from the spatial direction (θ,ϕ), the expression for the total effective area is

$$A_e=A_{xy}\cos\theta+A_{xz}\sin\phi\sin\theta+A_{yz}\cos\phi\sin\theta.\tag{29}$$

Therefore, for any spatial observation region $O = \{\theta_1 \leqslant \theta \leqslant \theta_2; \phi_1 \leqslant \phi \leqslant \phi_2\}$, the average gain limit of the 3D array normalized to a 2D array of the same aperture size is

$$\begin{aligned} G &= \frac{\iint_D A_{e,3D} \sin\theta d\theta d\phi}{\iint_D A_{e,2D} \sin\theta d\theta d\phi} \\ &= \frac{\iint_D \left(A_{xy}\cos\theta + A_{xz}\sin\phi\sin\theta + A_{yz}\cos\phi\sin\theta\right)\sin\theta d\theta d\phi}{\iint_D A_{xy}\cos\theta\sin\theta d\theta d\phi} \\ &= 1 + \frac{A_{xz}\left(\cos\phi_1 - \cos\phi_2\right)\left[\theta_2 - \theta_1 - \frac{1}{2}\left(\sin 2\theta_2 - \sin 2\theta_1\right)\right]}{A_{xy}\left(\phi_2 - \phi_1\right)\frac{1}{2}\left(\cos 2\theta_1 - \cos 2\theta_2\right)} \\ &\quad + \frac{A_{yz}\left(\sin\phi_2 - \sin\phi_1\right)\left[\theta_2 - \theta_1 - \frac{1}{2}\left(\sin 2\theta_2 - \sin 2\theta_1\right)\right]}{A_{xy}\left(\phi_2 - \phi_1\right)\frac{1}{2}\left(\cos 2\theta_1 - \cos 2\theta_2\right)}, \end{aligned} \tag{30}$$

and the average gain of the 3D array over half space can be approximated by

$$G = 1 + \frac{A_{xz} + A_{yz}}{A_{xy}}. \tag{31}$$

Thus, we can approximate (23), i.e., the Hannan limitation for finite-size 3D arrays, from the gain perspective as follows:

$$\eta_{3D} = \frac{N_{2D}}{N_{3D}}\left(1 + \frac{A_{xz} + A_{yz}}{A_{xy}}\right)\eta_{2D}, \tag{32}$$

where η_{2D} represents the original Hannan limitation for 2D arrays. N_{3D} and N_{2D} represent the total number of antennas of finite-size 3D and 2D arrays, respectively.

For practical base station antenna arrays, the horizontal hemispace scanning gain is often more important than the vertical hemispace scanning gain. This is because, in real communication scenarios, users are usually randomly distributed in the horizontal plane. However, in the vertical plane, apart from special scenarios such as base stations near high-rise buildings, the demand for wide-range vertical beamforming is rare. Therefore, considering horizontal hemispace scanning ($\theta_1 = 0, \theta_2 = \frac{\pi}{2}; \phi_1 = \phi_2 = \frac{\pi}{2}$), the average gain of the 3D array, normalized to that of a 2D array with the same aperture size, is

$$G = 1 + \frac{A_{xz}}{A_{xy}}. \tag{33}$$

In the above analysis, we consider the projected area of the 3D antenna array in the observation direction as its effective aperture area. Please note that achieving such a gain is not going to significantly increase the system complexity or hardware cost. Though the proposed 3D array introduces a higher element count than its 2D counterpart, when implemented under a hybrid beamforming structure with a fixed number of RF chains, the increase in hardware and feeding network complexity is marginal; moreover, its fabrication can be achieved with simple supporting structures, maintaining a complexity level comparable to conventional 2D arrays. However, since the 3D array gain essentially comes from the additional projection area for non-broadside directions, the more users are distributed across the whole sector or close to the edge areas, the more benefits we can obtain from utilizing 3D arrays. In the subsequent simulation section, we validate the effectiveness of this method by examining the hemispherical average gain of actual 3D antenna arrays.

5 3D feasible region

As analyzed in (24), we assume that the excitation phase pair (α, β) produces a spatial beam propagating at an angle θ with respect to the z-axis in the first octant of space. The corresponding phase change induced by this beam as it propagates from the lower planar array to the upper planar array is expressed as $\delta_z = \frac{2\pi d_z}{\lambda}\cos\theta$. Meanwhile, the phase difference γ introduced between adjacent elements along the z-axis in the 3D array also corresponds to a spatial propagation direction at an angle ξ relative to the z-axis. Due to the potential mismatch between the angles ξ and θ, there will be a difference between the imposed phase shift and the phase shift for beam alignment, thus reducing the array gain. To quantify this effect, we rewrite the phase difference resulting from the mismatch between the upper and lower arrays as

$$\varphi = \gamma - \delta_z = \frac{2\pi d_z}{\lambda}\left(\cos\xi - \cos\theta\right), \tag{34}$$

where ξ represents the angle between the z-axis and the propagation direction determined by the imposed phase difference γ. The physical meaning of (34) is that when the beam direction dictated by the imposed phase difference γ (characterized by angle ξ) deviates from the intended beam direction (angle θ), this deviation results in a non-zero residual phase φ, indicating misalignment and subsequent performance degradation.

Assume that in a 3D antenna array structure, the radiation electric field amplitude for a single-layer 2D array is $|\boldsymbol{E}|$ (which is smaller than the radiation intensity of an individual 2D array structure due to stronger coupling in the 3D array). When the phase between the upper and lower array planes is perfectly matched (i.e., $\xi = \theta$), the radiated electric field intensity is $2|\boldsymbol{E}|$. In the presence of a phase mismatch φ, the total radiated electric field intensity becomes $\left|1+e^{j\varphi}\right||\boldsymbol{E}|$, resulting in the radiated energy being $\left|1+e^{j\varphi}\right|^2 = 2+2\cos\varphi$ times the initial energy. Please note that our theory can be easily extended from a two-layer 3D antenna array to a multi-layer 3D array scenario. When the 3D array consists of L_z layers, the expression $\left|1+e^{j\varphi}\right|$ needs to be modified to $\left|\sum_{l=1}^{L_z} e^{jl\varphi}\right|$, with the subsequent analysis remaining the same. From the energy perspective, we introduce an attenuation threshold t such that $t = \left|1+e^{j\varphi_t}\right| = \sqrt{2+2\cos\varphi_t}$. When the electric field intensity exceeds t, it is considered a feasible beam; otherwise, it is deemed an infeasible beam. From the definition of the energy threshold t, it can be derived that

$$\cos\varphi_t = \frac{t^2-2}{2}. \tag{35}$$

By combining (34) and (35), we can derive that under the condition of a fixed phase shift along the z-axis, the boundary of θ that satisfies the amplitude threshold t is given by

$$\cos\left[\frac{2\pi d_z}{\lambda}\left(\cos\xi-\cos\theta\right)\right] = \frac{t^2-2}{2}, \tag{36}$$

which can be further decomposed into two boundary conditions for θ:

$$\begin{aligned}
\cos\theta_- - \cos\xi &= \frac{\lambda}{2\pi d_z}\arccos\left(\frac{t^2-2}{2}\right),\\
\cos\xi - \cos\theta_+ &= \frac{\lambda}{2\pi d_z}\arccos\left(\frac{t^2-2}{2}\right),
\end{aligned} \tag{37}$$

and the corresponding feasible θ region can be formulated as

$$\begin{aligned}
\theta \geqslant \theta_- &= \arccos\left[\cos\xi + \frac{\lambda}{2\pi d_z}\arccos\left(\frac{t^2-2}{2}\right)\right],\\
\theta \leqslant \theta_+ &= \arccos\left[\cos\xi - \frac{\lambda}{2\pi d_z}\arccos\left(\frac{t^2-2}{2}\right)\right],
\end{aligned} \tag{38}$$

which is shown in Figure 5.

From the derivation of the 2D Hannan limitation, we know that the radiation direction of a 2D array and the conical angles (μ,ν) with respect to the x and y coordinate axes satisfy the relationship $\sin^2\theta = \cos^2\mu + \cos^2\nu$. Therefore, the feasible region for the planar phase set (α,β) is given by

$$\begin{cases}
\cos^2(\mu)+\cos^2(\nu) \geqslant \sin^2(\theta_-),\\
\cos^2(\mu)+\cos^2(\nu) \leqslant \sin^2(\theta_+),
\end{cases} \tag{39}$$

which can be expanded as

$$\begin{cases}
\left(\frac{\alpha\lambda}{2\pi d_x}\right)^2 + \left(\frac{\beta\lambda}{2\pi d_y}\right)^2 \geqslant 1 - \left[\cos\xi + \frac{\lambda}{2\pi d_z}\arccos\left(\frac{t^2-2}{2}\right)\right]^2,\\
\left(\frac{\alpha\lambda}{2\pi d_x}\right)^2 + \left(\frac{\beta\lambda}{2\pi d_y}\right)^2 \leqslant 1 - \left[\cos\xi - \frac{\lambda}{2\pi d_z}\arccos\left(\frac{t^2-2}{2}\right)\right]^2.
\end{cases} \tag{40}$$

The above expansion is due to $\cos\mu = \frac{\alpha\lambda}{2\pi d_x}$ and $\cos\nu = \frac{\beta\lambda}{2\pi d_y}$. From (40), we can see that the general feasible region for a fixed amplitude parameter t forms a ring shape, as illustrated in Figure 6, where we set $d_x = d_y = d_z = \frac{\lambda}{2}$.

In the following, we will analyze UPA arrays with $d = d_x = d_y \leqslant \frac{\lambda}{2}$. In this case, the feasible region boundary simplifies from a more general elliptical shape to a more easily analyzable circular shape. Based on the above discussions, for any given phase shift parameter γ and amplitude attenuation parameter t, we can derive the analytical expressions for the area of the feasible region in the (α,β) plane, as well as the inner and outer radii of this area.

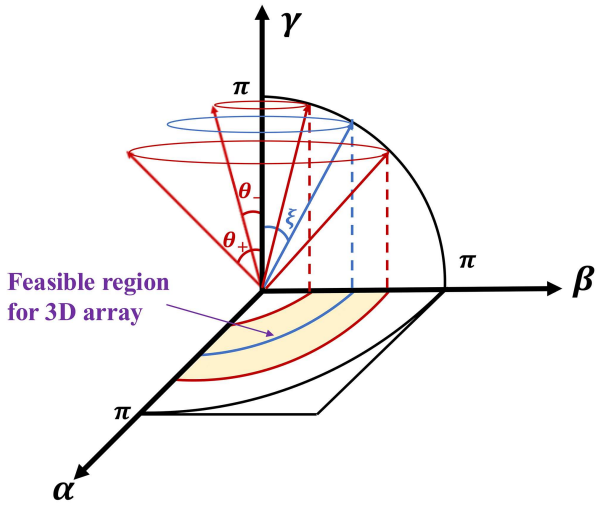

Figure 5 (Color online) The relationship between the planar feasible region and the radiation direction of 3D arrays.

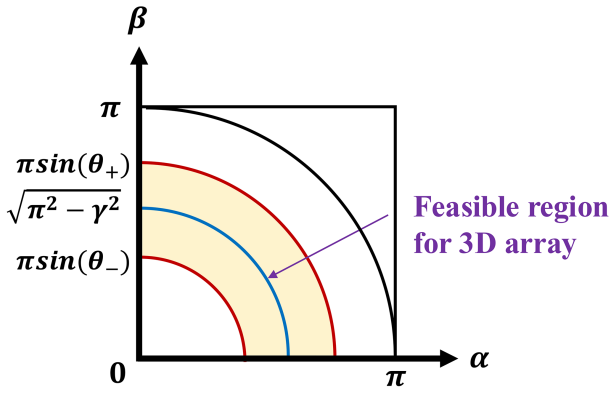

Figure 6 (Color online) Planar feasible region for fixed amplitude parameter t with $d_x = d_y = d_z = \frac{\lambda}{2}$.

Theorem 3. The feasible region of a 2-layer infinite 3D array for a fixed ξ is

$$\begin{aligned} r_- &= \sqrt{\left(\frac{2\pi d}{\lambda}\right)^2 - \left[\min\left(\frac{2\pi d}{\lambda}\cos\xi + \arccos\left(\frac{t^2-2}{2}\right), \frac{2\pi d}{\lambda}\right)\right]^2}, \\ r_+ &= \sqrt{\left(\frac{2\pi d}{\lambda}\right)^2 - \left[\max\left(\frac{2\pi d}{\lambda}\cos\xi - \arccos\left(\frac{t^2-2}{2}\right), 0\right)\right]^2}, \\ S(\gamma, t) &= \frac{2\pi^2 d}{\lambda}\cos\xi \arccos\left(\frac{t^2-2}{2}\right). \end{aligned} \tag{41}$$

From the above theorem, we can derive the normalized 3D feasible volume by integrating γ with the corresponding feasible region area,

$$V(t) = \frac{1}{\pi^3}\int_0^{\pi} S(\gamma, t)d\gamma. \tag{42}$$

However, although we have theoretically demonstrated that the feasible plane region where a 3D array can generate a relatively concentrated radiation beam follows a ring shape, it is not the case that for all values of γ, the upper and lower bounds of the feasible range are simultaneously within the first quadrant. Specifically, for certain settings of γ that make ξ close to 0° or 90° (corresponding to $\gamma = \frac{2\pi d_z}{\lambda}$ and $\gamma = 0$, respectively), θ_- and θ_+ do not both fall within the range of 0° to 90°. This requires further detailed investigation. Specifically, we analyze the joint feasible range of (α, β) in the following three cases.

5.1 Around z axis

When the beamforming angle ξ is small and around the z-axis, the corresponding left boundary θ_- may fall within the second quadrant. In this case, the relationship $\cos\theta_- = \cos\xi + \frac{\lambda}{2\pi d_z}\arccos(\frac{t^2-2}{2})$ no longer holds. For example, when $\xi_- = 0$, for large threshold values t, the result of the above equation may be greater than 1, which cannot represent the physical boundary between the feasible range and the z-axis. However, we observe that since $\xi \geqslant 0$ and the feasible range exhibits widening in both directions with respect to the beamforming direction specified by ξ, the right boundary θ_+ must be greater than the left boundary θ_-. Thus, the planar feasible range defined by θ_+ is guaranteed to include the planar feasible range corresponding to θ_-. Considering that we only consider the cases where α and β are within the range $[0, \pi]$, the final planar feasible range in this situation is constrained by the x-axis, y-axis, and $\frac{(\alpha^2+\beta^2)\lambda^2}{(2\pi d)^2} \leqslant \sin^2\theta_+$. It forms a quarter-circle within the first quadrant, as shown in region 1 of Figure 7.

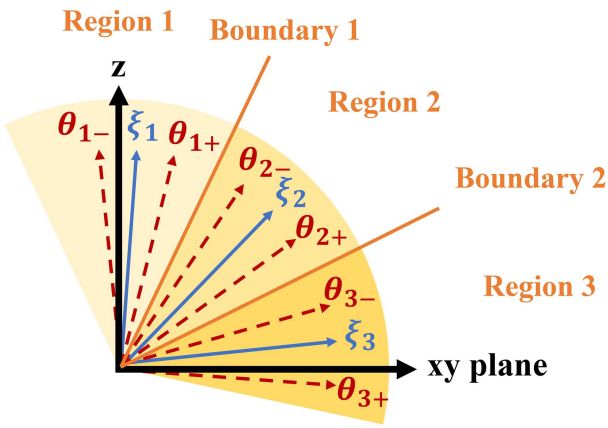

Figure 7 (Color online) Different planar feasible region cases dependent on ξ.

5.2 Medium case

We have already discussed this typical situation in our previous analysis of the planar feasible range for a 3D antenna array and its comparison with the feasible range of planar arrays, as shown in region 2 of Figure 7. Please note that in this case, the feasible angular width of the planar beamforming, i.e., $\theta_+ - \theta_-$, is determined by t. Larger values of t result in narrower feasible angular widths.

5.3 Around xy plane

In contrast to the case discussed in Section 5.1, we will now consider the situation that the beamforming angle ξ is close to 90° and lies around the xy plane (corresponding to a near-zero phase shift γ along the z-axis). In this scenario, the corresponding right boundary θ_+ may fall within the fourth quadrant. Please note that although the relationship $\cos\theta_+ = \cos\xi - \frac{1}{\pi}\arccos(\frac{t^2-2}{2})$ still holds, we cannot consider the integration domain in the same way as in the second-class classical case where we set $\frac{(\alpha^2+\beta^2)\lambda^2}{(2\pi d)^2} \leqslant \sin^2\theta_+$ as an upper bound. To determine the range of the planar feasible region in this case, we further divide it into two scenarios: $\frac{(\alpha^2+\beta^2)\lambda^2}{(2\pi d)^2} \leqslant 1$ and $\frac{(\alpha^2+\beta^2)\lambda^2}{(2\pi d)^2} > 1$.

Firstly, the region satisfying $\sin^2\theta_- \leqslant \frac{(\alpha^2+\beta^2)\lambda^2}{(2\pi d)^2} \leqslant 1$ is feasible. The underlying physical phenomenon is that the beamforming direction formed by the (α, β) phase set lies within the first octant of the 3D space. However, as shown in region 3 of Figure 7, when θ is between 90° and θ_+, the corresponding physical phenomenon is that the beamforming direction lies outside the first octant. This indicates that at the 90-degree boundary, there is still a residual energy attenuation margin. Therefore, some points in the region where $\frac{(\alpha^2+\beta^2)\lambda^2}{(2\pi d)^2}$ is greater than 1 are also feasible. The area of this region can be estimated as the plane feasible region corresponding to $\sin^2\theta_+ \leqslant \frac{(\alpha^2+\beta^2)\lambda^2}{(2\pi d)^2} \leqslant 1$ based on the symmetry, but its spatial radiation direction cannot be accurately controlled. Thus it has limited practical application significance.

5.4 Number and boundaries of feasible regions

Based on the above analysis, we can further derive a set of 3D phase settings that cover the entire space for a given threshold. Specifically, as shown in Figure 7, we divide the 3D space into different regions, each connected end to end. When we need to radiate energy into the 3D space, we can select the corresponding ξ parameter based on the elevation angle and the corresponding (α, β) parameters based on the azimuth angle. Since the main new feature of the 3D array is its ξ parameter, we focus on further research and design for this parameter.

Assuming that under a given attenuation threshold t, we need to cover the entire space with P discrete ξ. Specifically, we determine the first codeword ξ_1 by setting $\theta_{1-} = 0$. Subsequently, we determine $\xi_2, \ldots, \xi_P$ sequentially by setting $\theta_{p-1,+} = \theta_{p,-}$ until $\theta_{P,+} > \frac{\pi}{2}$. From (38), we have

$$\begin{aligned} \theta_{p-1,+} &= \arccos\left[\cos\xi_{p-1} - \frac{\lambda}{2\pi d_z}\arccos\left(\frac{t^2-2}{2}\right)\right], \\ \theta_{p,-} &= \arccos\left[\cos\xi_p + \frac{\lambda}{2\pi d_z}\arccos\left(\frac{t^2-2}{2}\right)\right]. \end{aligned} \tag{43}$$

By setting $\theta_{p-1,+} = \theta_{p,-}$, we have $\cos\xi_p = \cos\xi_{p-1} - \frac{\lambda}{\pi d_z}\arccos(\frac{t^2-2}{2})$. Moreover, since the first ξ can be determined by $\cos\xi_1 = \cos\theta_{1-} - \frac{\lambda}{2\pi d_z}\arccos(\frac{t^2-2}{2}) = 1 - \frac{\lambda}{2\pi d_z}\arccos(\frac{t^2-2}{2})$, we have

$$\cos\xi_p = 1 - \frac{(2p-1)\lambda}{2\pi d_z}\arccos\left(\frac{t^2-2}{2}\right). \tag{44}$$

The final spatial region P can be classified into two scenarios: (1) $\left\{\xi_P \leqslant \frac{\pi}{2}, \theta_{P,+} \geqslant \frac{\pi}{2}\right\}$; (2) $\left\{\theta_{P-1,+} \leqslant \frac{\pi}{2};, \xi_P \geqslant \frac{\pi}{2}\right\}$. And the corresponding ranges for P in the above two scenarios are

$$\begin{cases} 2P-1 \leqslant \frac{2\pi d_z}{\lambda\arccos\left(\frac{t^2-2}{2}\right)} \leqslant 2P, \\ 2P-2 \leqslant \frac{2\pi d_z}{\lambda\arccos\left(\frac{t^2-2}{2}\right)} \leqslant 2P-1, \end{cases} \tag{45}$$

and the total number of feasible regions P can be written as

$$P = \left\lfloor \frac{2\pi d_z}{2\lambda\arccos(\frac{t^2-2}{2})} \right\rfloor + 1. \tag{46}$$

To summarize, the feasible region analysis connects the spatial radiation directions of 3D arrays with their excitation settings, delineating the range of phased excitation required to generate desired directional spatial beams. In practical antenna design and beamforming implementations, we can apply beamforming feasible region analysis to guide how we are going to set the phase parameters for excitations, i.e., (α, β, γ). This is crucial for practical antenna design, as it allows engineers to tailor the radiation pattern to specific application requirements, such as focusing energy in a particular direction for long-distance communication or spreading energy over a wider area for coverage enhancement.

6 Numerical results

In this section, simulation results are presented to validate our theories and evaluate the performance of the proposed 3D array. The specific configurations are as follows: the communication system is assumed to operate at 1.6 GHz. The array is composed of identical printed dipole antennas, which are printed on an FR-4 substrate measuring 12.2 mm × 78 mm, and the dimensions of each dipole element are 1 mm × 71.5 mm. The dipole antennas are arranged along the y-axis at a fixed half-wavelength spacing, but the spacing along the x-axis is variable. For array simulations with a fixed array aperture area of $L_x \times L_y$, we maintain the antenna spacing at 0.5λ along the y-axis and set the antenna spacing along the x-axis as $\frac{L_x}{M-1}$, where M is the number of antennas along the x-axis. Regarding the 3D array topology, to comprehensively validate the radiation efficiency and array gain theories proposed in this paper, we consider the following configurations. For simulations of radiation efficiency, we adopt the double-layer array topology with vertically aligned radiating element pairs as illustrated in Figure 4. For simulations evaluating the array gain, to verify that the gain limit is determined solely by the projected area of the array, we consider two different 3D array structures as depicted in Figure 8, which differ in antenna element arrangements but share an identical projected area during radiation. All the simulations are modeled and conducted using commercial electromagnetic full-wave simulation software CST Studio Suite.

Figure 9 shows the 75-degree spatial radiation beams of 2D and 3D arrays with the same aperture size of $2\lambda \times 2\lambda$ (where the y-axis is the broadside direction). It can be observed that the 3D array is able to focus the radiated energy better than the traditional 2D array when performing large-angle radiation, achieving a narrower spatial beam and better array performance. The comparison reveals that the array gain derived from the conventional array is 13.5, whereas our proposed model yields a higher gain of 24.9, resulting in a gain increase of 84%.

Figure 10 displays the average radiation efficiency for 2D and 3D arrays with different inter-layer spacing configurations. It can be observed that Hannan limitation is well applicable for large 2D arrays, which aligns with the simulation and measurement results reported in [48, 49]. Additionally, the proposed theoretical radiation efficiency limit for finite-dimensional 2D arrays consistently remains above that of the actual 2D arrays. It also decreases with increasing array size and ultimately converges to the Hannan limitation. In terms of 3D arrays, due to the inclusion of a larger number of antenna elements and the corresponding coupling effects, the overall efficiency of 3D arrays is lower than that of equivalent aperture 2D arrays. Moreover, the proposed 3D Hannan limitation approximation formula (32) provides a tight efficiency upper bound on radiation for large 3D arrays.

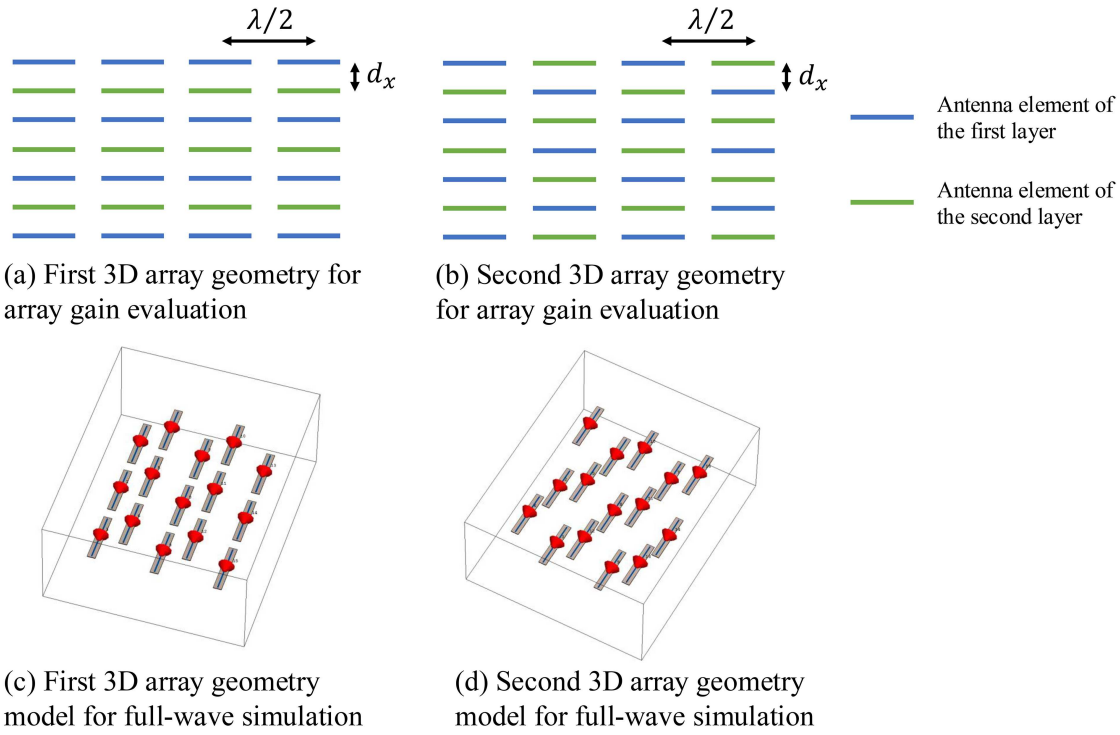

Figure 8 (Color online) 3D array geometry.

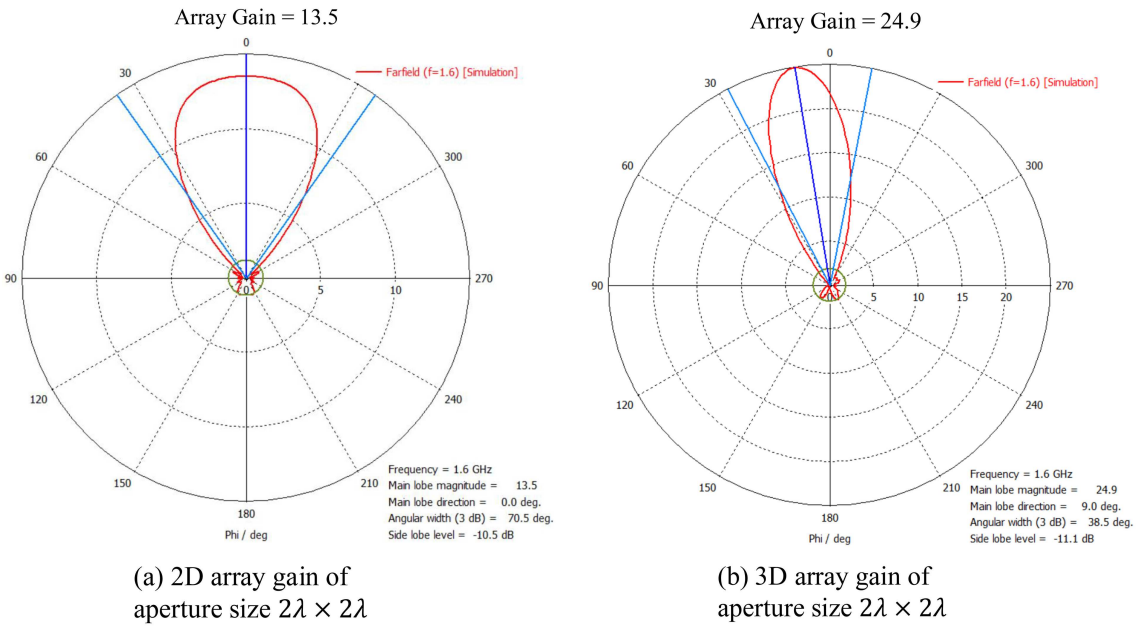

Figure 9 (Color online) Spatial beams for 2D and 3D arrays with identical aperture size.

Figure 11 shows the variation of the hemispace average array gain of 3D arrays as the inter-layer spacing increases. It can be seen that the antenna arrays exhibit local minimum points in average array gain at spacings of 0.1λ, 0.5λ, and 1λ. The first point is due to the strong coupling effect and the rest two points reflect the impact of the coherent energy cancellation effect introduced by the reflection effect between the two-layer planar arrays (due to the π phase shift introduced by perfect electrical conductor reflection, the array gain decreases for inter-layer spacings that are multiples of 0.5λ, and the proportion of reflected energy increases). Therefore, internal electromagnetic effects should be considered for the optimal geometric configuration of 3D arrays, with the spacing between layers set as odd multiples of 0.25λ.

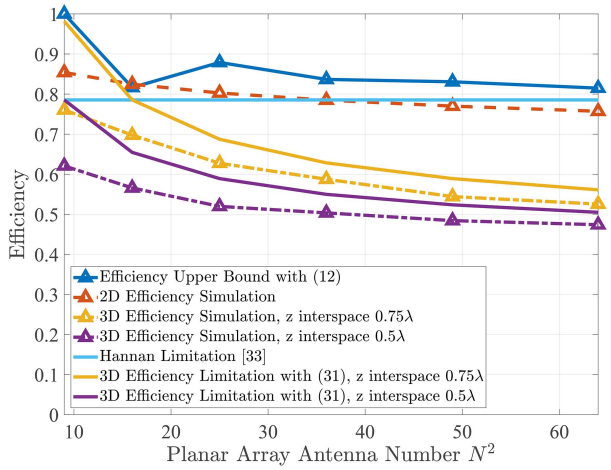

Figure 10 (Color online) Radiation efficiency for 2D/3D arrays with 0.5λ spacing.

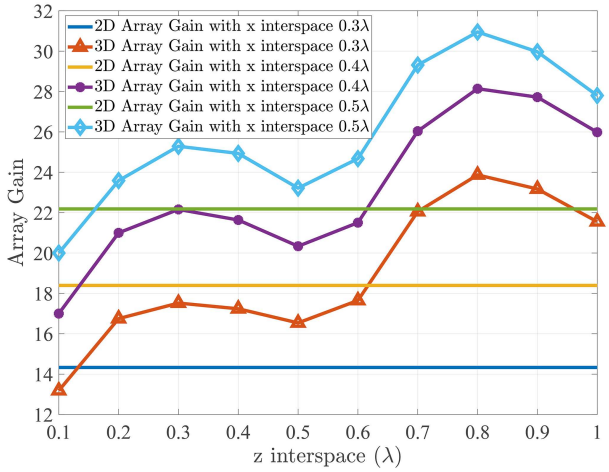

Figure 11 (Color online) Average array gains of 3D array over half-space with different inter-layer spacings.

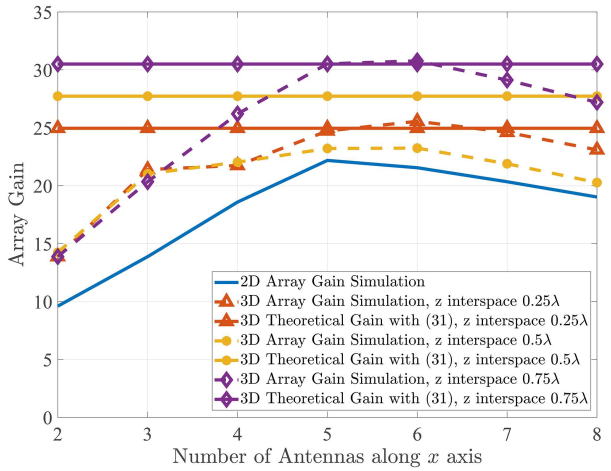

Figure 12 (Color online) Average array gains of the 3D array (Figure 8(a) geometry) over half-space with fixed aperture area.

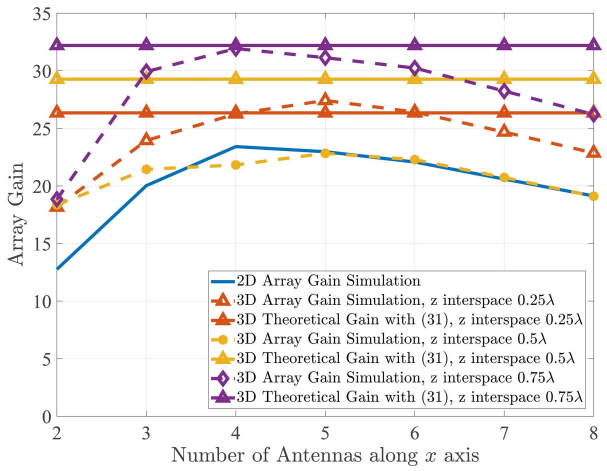

Figure 13 (Color online) Average array gains of the 3D array (Figure 8(b) geometry) over half-space with fixed aperture area.

Figure 12 shows the average array gain for different numbers of antennas with a fixed aperture area of $2\lambda \times 2\lambda$. It is observed that the 3D array exhibits a more pronounced performance gain compared to the 2D array. Additionally, when the array antenna arrangement becomes overly dense, the array gain decreases as EM mutual coupling effects become increasingly evident, resulting in a lower radiation efficiency. Therefore, for the two-layer 3D array considered in this paper, there also exists an optimal choice for the horizontal spacing between antenna elements. This optimal configuration typically occurs when the spacing between elements in each layer of the 3D array is close to 0.5λ, resulting in a top view element spacing of 0.25λ: this sub-wavelength densification approach enhances performance.

Figure 13 shows the average array gain in the hemispace for the 3D antenna array structure presented in Figure 8(b) while maintaining $2\lambda \times 2\lambda$ aperture area. Compared to Figure 12, it can be seen that approximately the same maximum achievable gain is realized with different 3D array arrangements. This is because the projection area of these two structures is the same. However, due to the larger spacing between antennas in the arrangement shown in Figure 8(b), the maximum gain can be achieved with fewer antenna elements.

In conclusion, the above simulation results demonstrate our corresponding theoretical derivations. However, there will be some non-ideal hardware impairments in practice, such as antenna displacements and spatial correlation effects. For example, a 5% spatial displacement of antenna elements may cause the performance to degrade by about 6%. We will further investigate these non-ideal factors in future research and develop corresponding mitigation strategies.

Figure 14 shows the spatial radiation characteristics of a 3D array with an interlayer spacing of 0.5λ. Specifically,

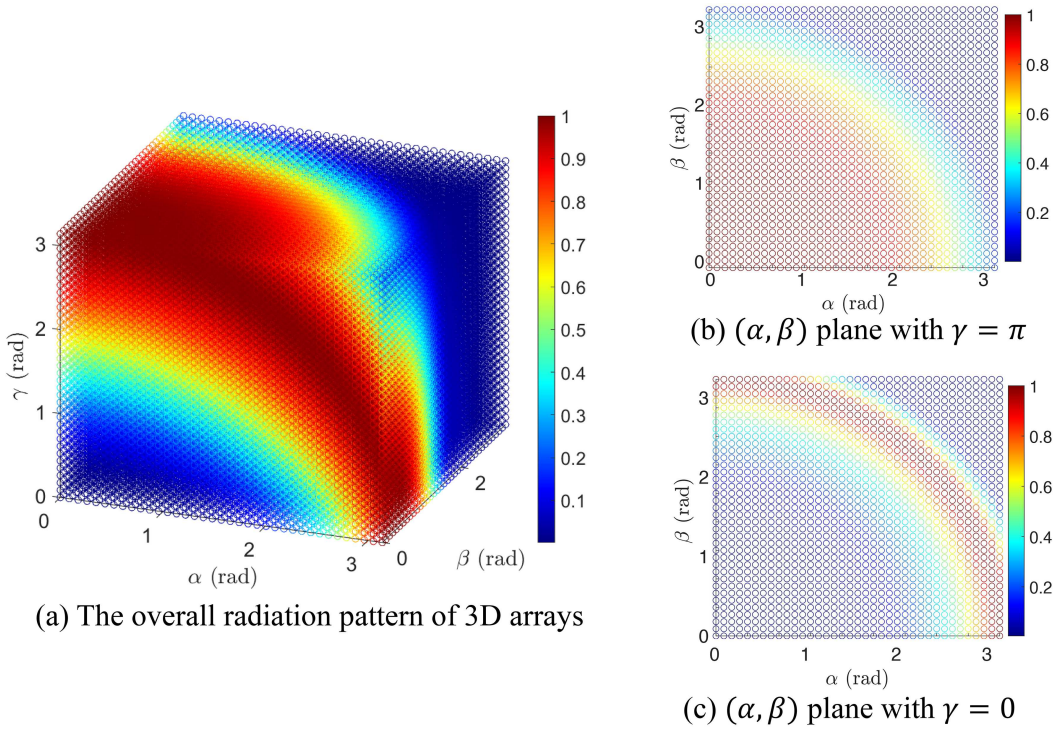

Figure 14 (Color online) Feasible region for a two-layer 3D array structure.

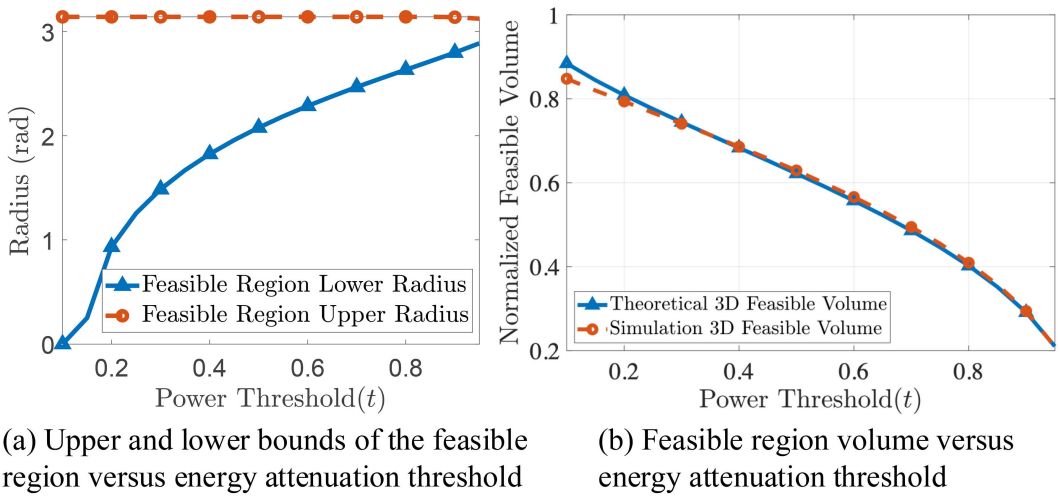

Figure 15 (Color online) Verification of feasible region analyses for a two-layer 3D array structure.

Figure 14(a) illustrates the normalized main beam intensity in space under different (α, β, γ) settings. From the figure, it is evident that for any given γ value, the region with higher spatial radiation energy corresponds to an annular region in the (α, β) plane. This is consistent with our previous feasible region theories of the 3D array radiation characteristics. Additionally, Figures 14(b) and (c) show the (α, β) plane for $\gamma = \pi$ and $\gamma = 0$ settings, respectively. These figures demonstrate that the feasible region of the 3D array varies with different γ settings, which need to be considered in practical applications.

Figure 15 presents the simulation results of the feasible region analysis for the 3D antenna array. Figure 15(a) shows the upper and lower bounds of the feasible region annulus for a fixed beamforming direction of $\cos\xi = \frac{1}{4}$ under different energy attenuation thresholds. It can be observed that in the region with higher energy attenuation thresholds, the radius of the feasible region boundary is approximately linear with the energy attenuation threshold. Figure 15(b) displays the relationship between the feasible region volume and the energy attenuation threshold, where it can be seen that the theoretically calculated feasible region volume in (42) matches the simulated feasible

region volume shown in Figure 14(a), verifying the correctness of the feasible region analysis theory.

7 Conclusion

In this paper, we extend the Hannan limitation theory on the radiation efficiency of infinite 2D planar arrays to finite-dimensional 2D arrays by leveraging the symmetry of the DFT and the relationship between reflection coefficients and mutual coupling coefficients. Furthermore, we investigate the efficiency and gain limits of a two-layer 3D array structure to obtain the achievable spatial array gain without increasing the planar aperture size. Specifically, results for both infinite and finite array cases are provided. Additionally, the spatial radiation and energy distribution characteristics of the considered two-layer 3D array structure are also investigated, presenting the feasible region of planar phase settings under a given energy attenuation threshold. Through simulations, we demonstrate the validity of our proposed theories for both efficiency and gain limits. Additionally, we verify the efficiency of our proposed 3D array structure for better spatial coverage and the theoretical analysis of the spatial radiation characteristics of the 3D antenna array.

Acknowledgements The work was supported by National Key R&D Program of China (Grant Nos. 2021YFA1000500, 2025ZD1301900, 2023YFB2904804), National Natural Science Foundation of China (Grant Nos. 62331023, 62394292), Zhejiang Provincial Science and Technology Plan Project (Grant No. 2024C01033), and Zhejiang University Global Partnership Fund.

References

1 Balanis C A. Antenna Theory: Analysis and Design. Hoboken: Wiley, 2016
2 Elliott R S. Beamwidth and directivity of large scanning arrays. Microwave J, 1964, 1: 74–82
3 Telatar E. Capacity of multi-antenna Gaussian channels. Trans Emerging Tel Tech, 1999, 10: 585–595
4 Tse D, Viswanath P. Fundamentals of Wireless Communication. Cambridge: Cambridge University Press, 2005
5 Paulraj A J, Gore D A, Nabar R U, et al. An overview of MIMO communications a key to gigabit wireless. Proc IEEE, 2004, 92: 198–218
6 Marzetta T L. Noncooperative cellular wireless with unlimited numbers of base station antennas. IEEE Trans Wireless Commun, 2010, 9: 3590–3600
7 Larsson E G, Edfors O, Tufvesson F, et al. Massive MIMO for next generation wireless systems. IEEE Commun Mag, 2014, 52: 186–195
8 Björnson E, Sanguinetti L, Wymeersch H, et al. Massive MIMO is a reality—What is next? Digital Signal Processing, 2019, 94: 3–20
9 Hoydis J, ten Brink S, Debbah M. Massive MIMO in the UL/DL of cellular networks: How many antennas do we need? IEEE J Sel Areas Commun, 2013, 31: 160–171
10 Wan Z, Gao Z, Gao F, et al. Terahertz massive MIMO with holographic reconfigurable intelligent surfaces. IEEE Trans Commun, 2021, 69: 4732–4750
11 Gan X, Huang C W, Yang Z H, et al. Fundamental channel coupling effects for integrated sensing and communication systems. Sci China Inf Sci, 2025, 68: 192301
12 Lou Y M, Jin L, Wang H M, et al. Multi-stream signals separation based on space-time-isomeric (SPATIO) array using metasurface antennas. Sci China Inf Sci, 2024, 67: 122301
13 Sun J X, Cheng Y J. Blindness-free beam scanning antenna with array of array architecture: principle, design, and experiment. Sci China Inf Sci, 2024, 67: 132301
14 Jiang C, Cong Y, Chen J, et al. Rethinking development and major research plans of Industrial Internet in China. Fundamental Res, 2024, 4: 3–7
15 Wei X, Wu D, Zhou L, et al. Cross-modal communication technology: a survey. Fundamental Res, 2025, 5: 2256–2267
16 Huang C, Zappone A, Alexandropoulos G C, et al. Reconfigurable intelligent surfaces for energy efficiency in wireless communication. IEEE Trans Wireless Commun, 2019, 18: 4157–4170
17 Tang W, Dai J Y, Chen M Z, et al. MIMO transmission through reconfigurable intelligent surface: system design, analysis, and implementation. IEEE J Sel Areas Commun, 2020, 38: 2683–2699
18 Wei L, Huang C, Alexandropoulos G C, et al. Channel estimation for RIS-empowered multi-user MISO wireless communications. IEEE Trans Commun, 2021, 69: 4144–4157
19 Bai X, Tan S, Mikki S, et al. Information-theoretic measures for reconfigurable metasurface-enabled direct digital modulation systems: an electromagnetic perspective. Progress Electromagn Res, 2024, 179: 1–18
20 Shi W, Xu W, You X, et al. Intelligent reflection enabling technologies for integrated and green internet-of-everything beyond 5G: communication, sensing, and security. IEEE Wireless Commun, 2023, 30: 147–154
21 Shi W, Yao J, Xu W, et al. Combating interference for over-the-air federated learning: a statistical approach via RIS. IEEE Trans Signal Process, 2025, 73: 936–953
22 Shi W, Yao J C, Xu J D, et al. Empowering over-the-air personalized federated learning via RIS. Sci China Inf Sci, 2024, 67: 219302
23 Xu J D, Yuen C, Huang C W, et al. Reconfiguring wireless environments via intelligent surfaces for 6G: reflection, modulation, and security. Sci China Inf Sci, 2023, 66: 130304
24 Zhang B, Xu K, Xia X, et al. Sum-rate enhancement for RIS-assisted movable antenna systems: joint transmit beamforming, reflecting design, and antenna positioning. IEEE Trans Veh Technol, 2025, 74: 4376–4392
25 Xu J, Xu W, Yuen C. On performance of distributed RIS-aided communication in random networks. IEEE Trans Wireless Commun, 2024, 23: 18254–18270
26 Xu W, Yang Z, Ng D W K, et al. Edge learning for B5G networks with distributed signal processing: semantic communication, edge computing, and wireless sensing. IEEE J Sel Top Signal Process, 2023, 17: 9–39
27 Zhang H, Zhang H, Di B, et al. Holographic integrated sensing and communication. IEEE J Sel Areas Commun, 2022, 40: 2114–2130
28 Wei L, Huang C, Alexandropoulos G C, et al. Multi-user holographic MIMO surfaces: channel modeling and spectral efficiency analysis. IEEE J Sel Top Signal Process, 2022, 16: 1112–1124
29 An J, Xu C, Ng D W K, et al. Stacked intelligent metasurfaces for efficient holographic MIMO communications in 6G. IEEE J Sel Areas Commun, 2023, 41: 2380–2396
30 Ji R, Chen S, Huang C, et al. Extra DoF of near-field holographic MIMO communications leveraging evanescent waves. IEEE Wireless Commun Lett, 2023, 12: 580–584
31 Pizzo A, Sanguinetti L, Marzetta T L. Fourier plane-wave series expansion for holographic MIMO communications. IEEE Trans Wireless Commun, 2022, 21: 6890–6905
32 Huang C, Ji R, Wei L, et al. Electromagnetic channel modeling theory and approaches for holographic MIMO wireless communications. J Electron Inf Techn, 2022, 47: 1–11

33 Nemati M, Park J, Choi J. RIS-assisted coverage enhancement in millimeter-wave cellular networks. IEEE Access, 2020, 8: 188171
34 Gan X, Zhong C, Huang C, et al. Multiple RISs assisted cell-free networks with two-timescale CSI: performance analysis and system design. IEEE Trans Commun, 2022, 70: 7696–7710
35 Gong T, Gavriilidis P, Ji R, et al. Holographic MIMO communications: theoretical foundations, enabling technologies, and future directions. IEEE Commun Surv Tutorials, 2023, 26: 196–257
36 Ji R, Huang C, Chen X, et al. Electromagnetic hybrid beamforming for holographic MIMO communications. IEEE Trans Wireless Commun, 2024, 23: 15973–15986
37 Han L, Yin H. Superdirectivity-enhanced wireless communications: a multi-user perspective. 2023. ArXiv:2307.06958
38 Huang C, Hu S, Alexandropoulos G C, et al. Holographic MIMO surfaces for 6G wireless networks: opportunities, challenges, and trends. IEEE Wireless Commun, 2020, 27: 118–125
39 Björnson E, Chae C-B, Heath R W, et al. Towards 6G MIMO: massive spatial multiplexing, dense arrays, and interplay between electromagnetics and processing. 2024. ArXiv:2401.02844
40 Migliore M D. Horse (electromagnetics) is more important than horseman (information) for wireless transmission. IEEE Trans Antennas Propagat, 2019, 67: 2046–2055
41 Yuan S S A, He Z, Chen X, et al. Electromagnetic effective degree of freedom of an MIMO system in free space. Antennas Wirel Propag Lett, 2022, 21: 446–450
42 Wan Z, Zhu J, Zhang Z, et al. Mutual information for electromagnetic information theory based on random fields. IEEE Trans Commun, 2023, 71: 1982–1996
43 Mikki S. The Shannon information capacity of an arbitrary radiating surface: an electromagnetic approach. IEEE Trans Antennas Propagat, 2023, 71: 2556–2570
44 Franceschetti M. Wave Theory of Information. Cambridge: Cambridge University Press, 2017
45 Askarian A, Wu K. Aperture-shared radiation surface: a promising technique for multifunctional antenna array development. Electromagn Sci, 2023, 1: 0030082
46 Wang Z, Wu Q. Extension of Hannan's limit: evaluation and enhancement of beam-scanning performance of planar phased arrays. Electromagn Sci, 2024, 2: 1–14
47 Hannan P. The element-gain paradox for a phased-array antenna. IEEE Trans Antennas Propagat, 1964, 12: 423–433
48 Kildal P S, Vosoogh A, Maci S. Fundamental directivity limitations of dense array antennas: a numerical study using Hannan's embedded element efficiency. Antennas Wirel Propag Lett, 2015, 15: 766–769
49 Yuan S S A, Chen X, Huang C, et al. Effects of mutual coupling on degree of freedom and antenna efficiency in holographic MIMO communications. IEEE Open J Antennas Propag, 2023, 4: 237–244
50 Wasylkiwskyj W, Kahn W. Efficiency as a measure of size of a phased-array antenna. IEEE Trans Antennas Propagat, 1973, 21: 879–884
51 Wasylkiwskyj W, Kahn W. Element patterns and active reflection coefficient in uniform phased arrays. IEEE Trans Antennas Propagat, 1974, 22: 207–212
52 Wasylkiwskyj W. Mutual coupling effects in semi-infinite arrays. IEEE Trans Antennas Propagat, 1973, 21: 277–285
53 Wasylkiwskyj W, Kahn W K. Mutual coupling and element efficiency for infinite linear arrays. Proc IEEE, 1968, 56: 1901–1907
54 Nuttall A H, Cray B A. Approximations to directivity for linear, planar, and volumetric apertures and arrays. IEEE J Ocean Eng, 2001, 26: 383–398
55 Costa B F, Abrao T. Closed-form directivity expression for arbitrary volumetric antenna arrays. IEEE Trans Antennas Propagat, 2018, 66: 7443–7448
56 Das S, Mandal D, Ghoshal S P, et al. Generalization of directivity expressions for antenna arrays. IEEE Trans Antennas Propagat, 2017, 65: 915–919
57 Song X, Fettweis G. On spatial multiplexing of strong line-of-sight MIMO with 3D antenna arrangements. IEEE Wireless Commun Lett, 2015, 4: 393–396
58 Hu S, Rusek F, Edfors O. Beyond massive MIMO: the potential of data transmission with large intelligent surfaces. IEEE Trans Signal Process, 2018, 66: 2746–2758
59 Yuan S S A, Wu J, Xu H, et al. Breaking the degrees-of-freedom limit of holographic MIMO communications: a 3-D antenna array topology. IEEE Trans Veh Technol, 2024, 73: 11276–11288
60 Meng H, Xin N, Qin H, et al. A recursive DRL-based resource allocation method for multibeam satellite communication systems. Chin J Elect, 2024, 33: 1286–1295
61 Wang C, Wang Z, Xu L, et al. Collaborative caching in vehicular edge network assisted by cell-free massive MIMO. Chin J Elect, 2023, 32: 1218–1229
62 An J, Yuen C, Xu C, et al. Stacked intelligent metasurface-aided MIMO transceiver design. IEEE Wireless Commun, 2024, 31: 123–131
63 Kahn W. Element efficiency: a unifying concept for array antennas. IEEE Antennas Propag Mag, 2007, 49: 48–56
64 Yang J, Cai W, Wu X. A high-order time domain discontinuous galerkin method with orthogonal tetrahedral basis for electromagnetic simulations in 3-D heterogeneous conductive media. Commun Comput Phys, 2018, 21: 1065–1089
65 Capek M, Jelinek L, Masek M. Finding optimal total active reflection coefficient and realized gain for multiport lossy antennas. IEEE Trans Antennas Propagat, 2021, 69: 2481–2493